



Measurement, modeling and simulation of wind turbulence in typhoon outer region



Lin Zhao ^{a,b,c}, Wei Cui ^{a,b,c,*}, Yaojun Ge ^{a,b,c}

^a State Key Lab of Disaster Reduction in Civil Engineering, Tongji University, Shanghai, 200092, China

^b Department of Bridge Engineering, College of Civil Engineering, Tongji University, Shanghai, 200092, China

^c Key Laboratory of Transport Industry of Bridge Wind Resistance Technologies, Tongji University, Shanghai, 200092, China

ARTICLE INFO

Keywords:

Typhoons
Turbulence
Non-Gaussian
Translation process
Non-Gaussian process simulation

ABSTRACT

Typhoon is one of the most destructive natural hazards, causing tremendous economic loss and fatalities every year all over the world. High-frequency wind observing tools have been deployed in many projects, which have been utilized in many recent studies to obtain data on typhoon winds, as well as turbulence. This study utilized field measurement data from the Xihoumen Bridge health monitoring system and examined the wind characteristics over water terrain at single point from four typhoons when their outer regions passed the bridge. This study firstly reviews the typhoon structure, which consists of two airflow circulations in horizontal and vertical directions. Results of this study suggest that the near ground wind turbulence characteristics should be analyzed for both directions separately. Next, the turbulence intensity, length scale, spectrum, and non-Gaussian features (skewness and kurtosis) are presented. Correlations among these parameters are also analyzed, and simplified mathematical models are introduced to quantify the correlation among various turbulence characteristics. Then, a Hermite-model based translation function method is used to simulate the non-Gaussian turbulences for different typhoon configurations. Gaussian turbulence neglecting skewness and kurtosis is also generated, and the comparison shows that non-Gaussian turbulence tends to have larger extreme gusts.

1. Introduction

Strong tropical cyclones (typhoons or hurricanes) are among the most destructive weather phenomena resulting strong winds and surge effect, which can cause severe damage to property and loss of life. In 2005, Hurricane Katrina caused 1833 fatalities and \$108 billion in property damage along the Gulf of Mexico coast. In 2013, Typhoon Haiyan landed Philippines, Vietnam and China sequentially. It was one of strongest recorded tropical cyclones, causing over 7000 fatalities and \$4.55 billion in property damage. As a result, the severity of the tropical cyclone threat has motivated researchers in the wind and civil engineering fields to conduct several on-going studies, aiming at accurately forecasting and simulating tropical cyclone activity from meso-scale to micro-scale in the geographical dimension and from near to distant future in the time dimension. The following section briefly reviews the most important models, currently employed for tropical cyclone simulation in wind engineering. “Tropical cyclone” also can be interpreted as “hurricane” for Atlantic Ocean or “typhoon” for Pacific Ocean depending on geographic location. However, because the study in paper is carried out near

northwestern Pacific coast, “typhoon” is used throughout this paper for consistency.

At first, typhoon intensity and translation were the major research focus, and several models, such as the single site method in Georgiou (1986) and Simiu and Scanlan (1986), and the full track model in Vickery et al. (2000a, b) were developed to simulate the typhoon intensity evolution and translation over the entire typhoon life-cycle. In later years, climate change effect on typhoons activity and consequent damage were also studied (Mudd et al., 2014; Cui and Caracoglia, 2016). During that time, several wind field models were proposed to calculate the wind speeds distribution for various typhoon intensities (Vickery et al., 2000b; Meng et al., 1995). Recently, Fang et al. (2018) introduced a novel analytical typhoon wind field model that considered height dependency and multi-field correlation.

Wind turbulence characteristics are another focus of fundamental wind engineering research (Davenport, 1961b). At early stage, attention was paid to the spectral features of synoptic winds in the atmosphere boundary layer, and many approximate turbulence spectra formulas were developed for structural design purpose (Kaimal et al., 1972;

* Corresponding author. 207 Wind Engineering Building, Tongji University , 1239 Siping Road, Shanghai, 200092, China.

E-mail address: cuiwei@tongji.edu.cn (W. Cui).

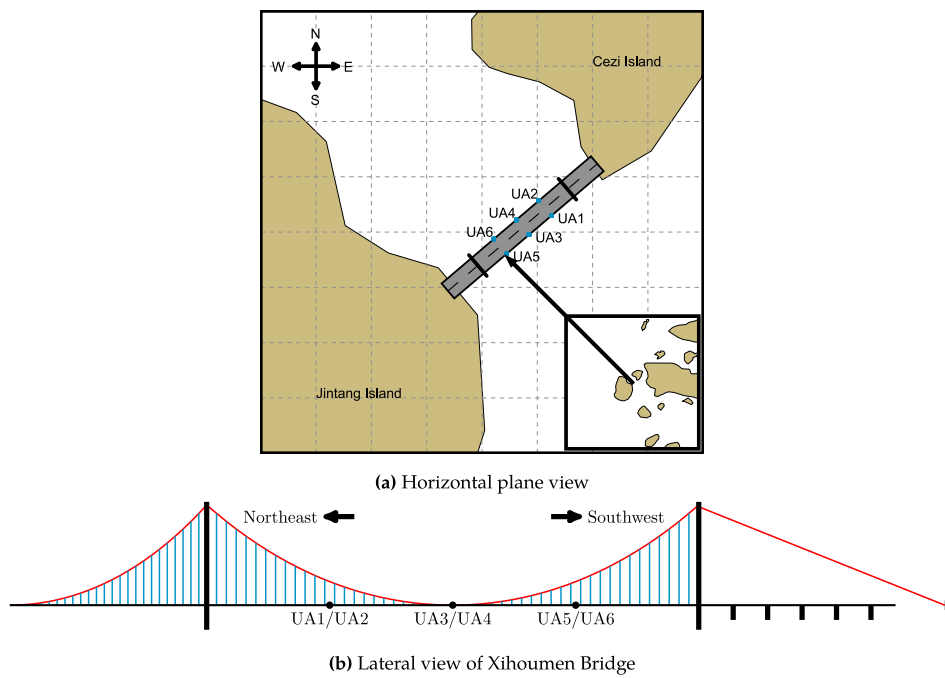


Fig. 1. Sketch of Xihoumen Bridge and the ultrasonic anemometer locations.

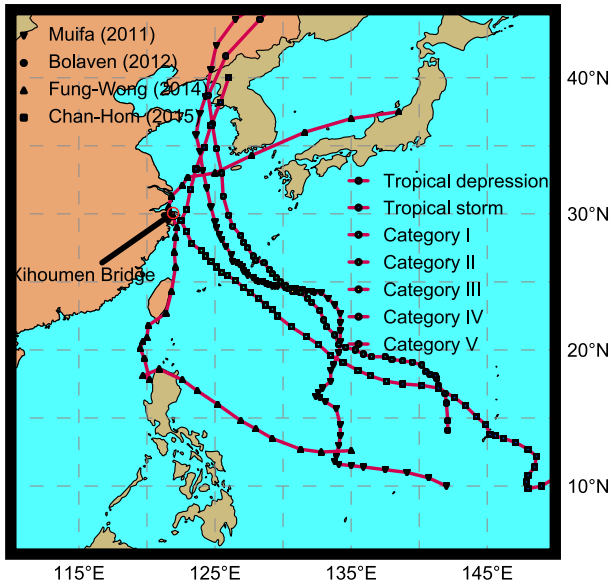
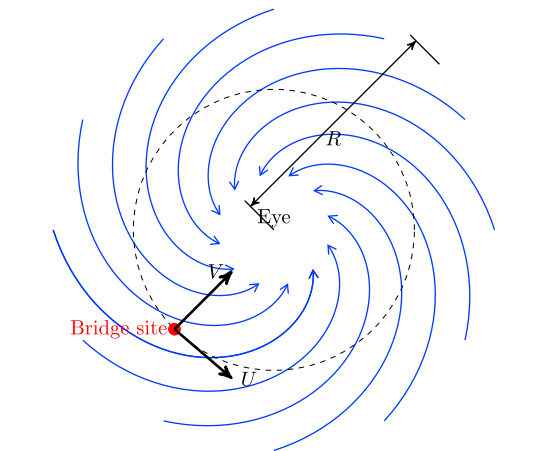
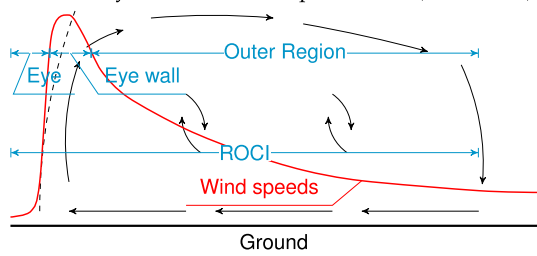


Fig. 2. Four typhoons affected Xihoumen Birdge from 2009 to 2016.

Davenport, 1961a; Von Karman, 1948). Recently, with the development of high-frequency wind observation facilities, many typhoon wind fields and turbulence characteristics have been recorded and reported in several studies (Li et al., 2015; Cao et al., 2009; Zhi et al., 2011). As a pioneering study, Cao et al. (2009) presented a full record of typhoon Maemi, which landed at Miyakojima Island of Okinawa Prefecture, Japan. It summarized typhoon wind turbulence characteristics through statistical measures (turbulence intensity, scale and etc.) and spectral comparison with a Von Kármán type spectrum. Li et al. (2015) compared turbulence characteristics of typhoons in the western Pacific and hurricanes in the Atlantic. Zhi et al. (2011) presented the field measurements of typhoon-generated wind characteristics on a super-tall building located in Guangzhou.



(a) Primary circulation of tropical storm (horizontal)



(b) Secondary circulation of tropical storm (vertical)

Fig. 3. Two circulations of tropical storm.

Based on these previous articles, typhoon wind turbulence characteristics can be roughly summarized as:

1. The turbulence intensity and integral length scale of typhoons are slightly higher than those of synoptic winds (Sharma and Richards, 1999). However, controversial statements can be found in other

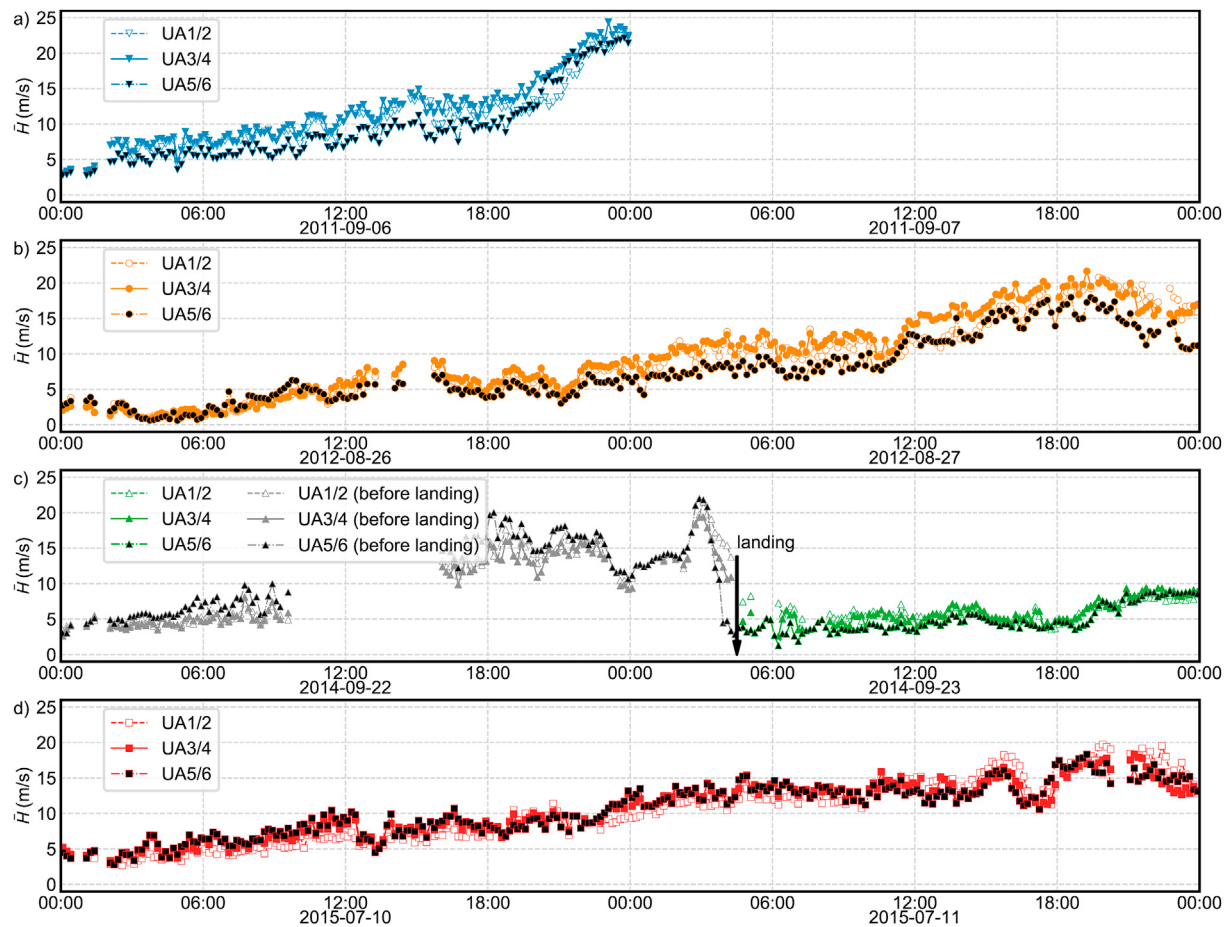


Fig. 4. Mean wind speeds at Xihoumen Bridge from four typhoon records (a: Typhoon Muifa, b: Typhoon Bolaven, c: Typhoon Fung-Wong, d: Typhoon Chan-Hom, Time Zone: UTC+8).

- literature, such as Masters et al. (2010), which believe that they share a considerable amount of similarity.
2. The turbulence spectra of typhoon winds generally follow the von Kármán spectrum type. However, several literatures (Yu et al., 2008; Schroeder et al., 2009) have reported that they have extra energy in the low-frequency range. Also, in the high-frequency inertial sub-range, some recorded typhoon turbulences don't satisfy Kolmogorov's second hypothesis, i.e., that slope rates are sometimes higher than $-\frac{5}{3}$ (Wang et al., 2017).
 3. For high-order moment of turbulence statistics such as skewness and kurtosis, controversial conclusions can be found in different literature. Cao et al. (2009) showed the variations of skewness and kurtosis for different mean speeds and concluded that the averaged skewness is 0 and kurtosis is close to 3. However, Li et al. (2015) compared variations of skewness with longitudinal turbulence intensities and concluded that turbulence speed distribution is different from a Gaussian distribution.

In these previously mentioned studies, more attention was focused on landing areas close to the typhoon center. However, due to typhoon's tremendous size, most damage occurs in its outer region, even though the wind speeds are lower than the center region. Also, it is important to understand typhoon wind turbulence characteristics in the outer regions, especially the non-Gaussian features compared with those of synoptic winds. From the viewpoint of statistical frequency, typhoon landings are very rare events, while events affected by a typhoon's outer regions are more frequent.

In this paper, we firstly analyze the basic wind turbulence characteristics over water terrain at single point, especially the non-Gaussian

statistical properties, from four strong and intermediate typhoons when their outer regions passed the wind measuring instruments located on East China Sea coast. In the second part of this paper, the non-Gaussian wind turbulence field for long-span bridges is simulated based on the wind characteristics analyzed in the first part using Hermite polynomial transformation. Compatibility between the non-Gaussian cross spectrum and the Hermite polynomial transfer function are also discussed.

2. Measurement site and instruments

The wind turbulences were recorded by ultrasonic anemometers, which is one part of the structural health monitoring system (SHMS) of the Xihoumen Bridge. This bridge is a suspension bridge with 1650 m main span linking Jintang and Cezi islands off the East China Sea coast, and is shown in Fig. 1a.

A total of 6 ultrasonic anemometers (UAs) are installed on the bridge. One UA is located on each side of the bridge girder at 1/4, 1/2 and 3/4 span by cantilever trusses with enough vertical space to avoid interference effects. The exact UA locations can be seen in Fig. 1a and b. The sampling rate of the UAs is 32 Hz, and the measuring range is 0–65 m/s. UAs can record wind turbulence speeds for 3 directions simultaneously: north, west, and upward (vertical). The anemometers are installed on lighting poles at a height of 6 m above the bridge deck surface.

3. Measured typhoon records

Since the installation of the SHMS, a total of 5 typhoons affected Xihoumen Bridge before 2016: Muifa in 2011, Bolaven in 2012, Tembin in 2012, Fung-Wong in 2014 and Chan-Hom in 2015. However, typhoon

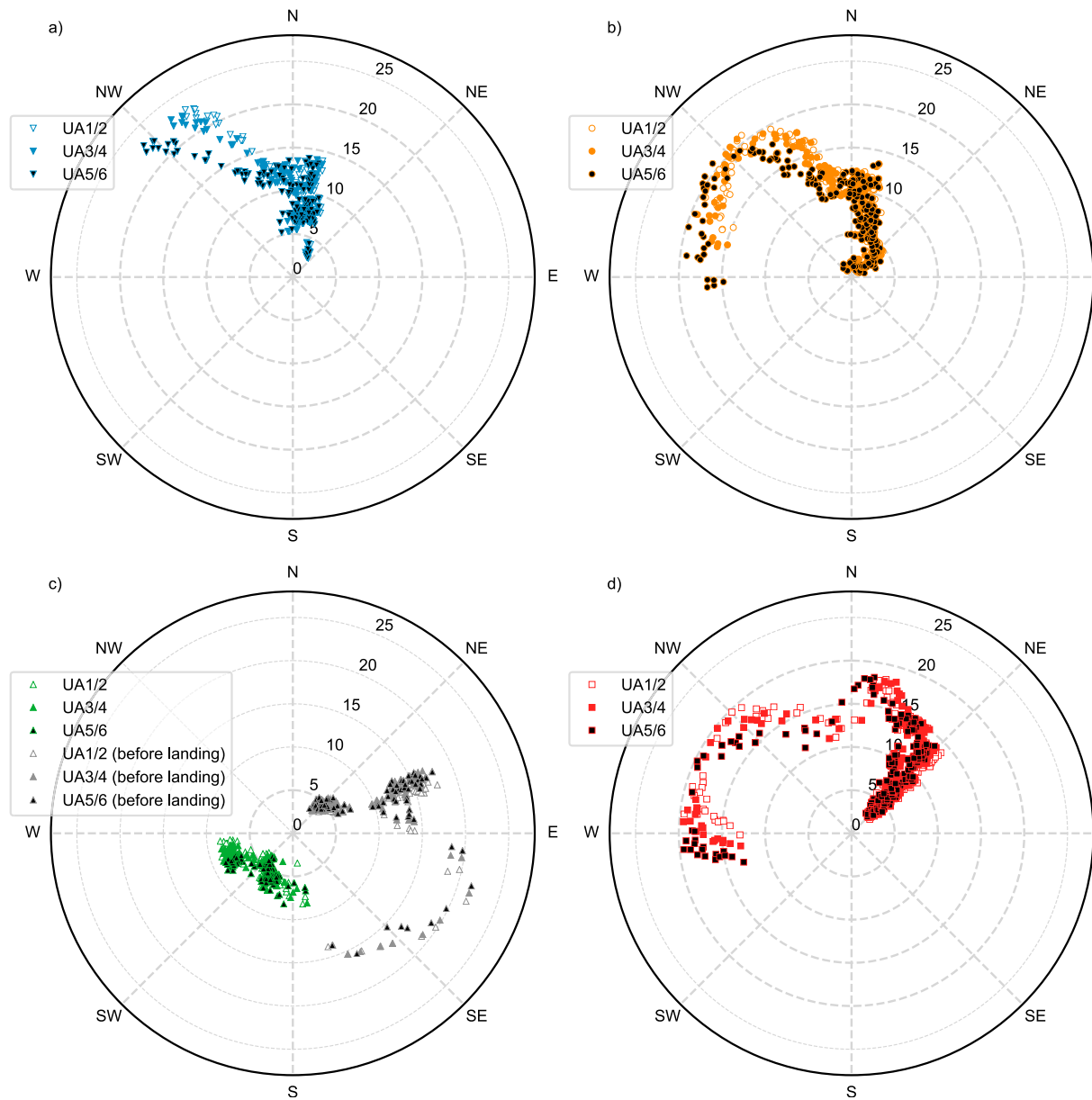


Fig. 5. Mean wind directions at Xihoumen Bridge from four typhoon records (a: Typhoon Muifa, b: Typhoon Bolaven, c: Typhoon Fung-Wong, d: Typhoon Chan-Hom).

Tembin and typhoon Bolaven were a special twin-typhoon system, and typhoon Tembin, the weaker one, was strongly affected by Typhoon Bolaven. The wind field and turbulence characteristics of typhoon Tembin were irregular and are excluded from this study. The exceptional wind turbulence of typhoon Tembin presents added researching value, and will be investigated in future study.

Fig. 2 shows the full tracks and the intensity evolution of the 4 typhoons. The data were extracted from the International Best Track Archive for Climate Stewardship (IBTrACS), which maintained by National Oceanic and Atmospheric Administration (NOAA), USA. IBTrACS is the most widely used global tropical cyclones database and has been endorsed by The World Meteorological Organization. In IBTrACS, typhoon activities are normally recorded every 6 h, represented as one symbol in Fig. 2. The color of the symbols demonstrates the typhoon intensity categories according to the Saffir-Simpson scale. Typhoon Bolaven was the strongest typhoon studied here, but they were all decayed to category I or tropical storm when they reached Xihoumen

Bridge.

Of the 4 analyzed typhoons, only tropical storm Fung-Wong landed on the Chinese mainland on September 23rd, 2014, and its closest distance to Xihoumen Bridge was 10.7 km. Just their outer region of the all other 3 typhoons affected the Chinese coastline. However, even without a typhoon landing, Xihoumen bridge was closed by the local transportation department to ensure the structural and transportation safety. As an example, typhoon Bolaven, whose closest distance was as far as 376.6 km, still forced Xihoumen Bridge to be closed for over 10 h. This further verifies the motivation of this study: it is necessary to study the wind characteristics of a typhoon's outer region and its effects on structural dynamic behavior. It should be mentioned that this study tries to build the relationship between typhoon macro structure (typhoon center location, wind field) and turbulence characteristic in term of numerical factors, rather than turbulence regularity in the atmospheric boundary layer.

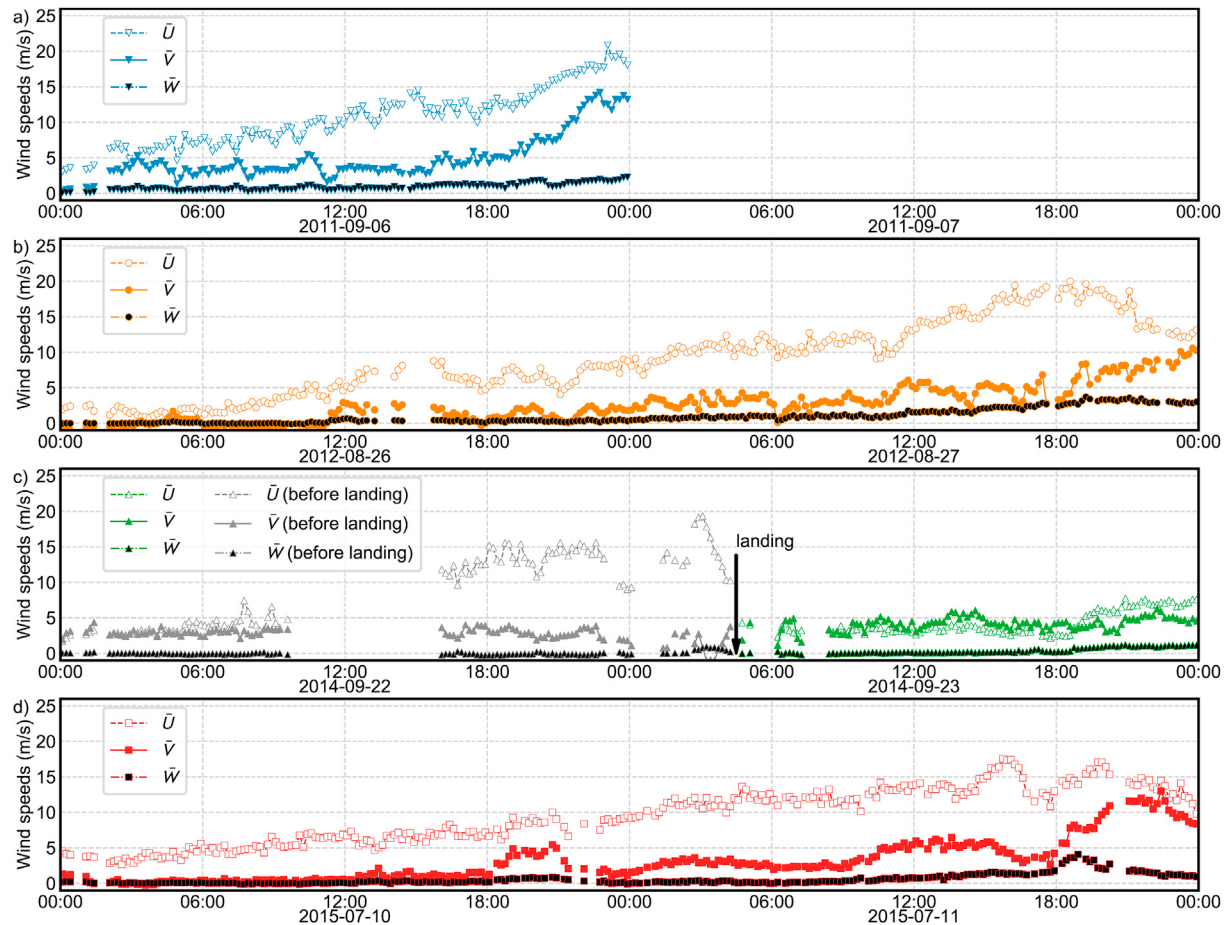


Fig. 6. Mean wind speeds at Xihoumen Bridge from four typhoon records in tangential, radial and vertical directions (a: Typhoon Muifa, b: Typhoon Bolaven, c: Typhoon Fung-Wong, d: Typhoon Chan-Hom, Time Zone: UTC+8).

4. Background of typhoon structures

Synoptic-scale winds such as monsoons have distinct features compared with mesoscale winds. Several well established turbulence and wind field models developed in the 20th century have been approved through various engineering applications. However, wind-field and turbulence characteristics of typhoons are still relatively unknown, and many research projects focusing on these characteristics are being undertaken around the world. It is necessary to review a typhoon's internal structure, which is the inherent driving force in its turbulent wind field.

A three-dimensional typhoon wind field can be divided into two components: "primary circulation" in the horizontal direction and "secondary circulation" in the vertical direction (Emanuel, 1986).

Primary circulation comprises rotating flow around the typhoon's eye, which dominates the surface wind field. As shown in Fig. 3a, this rotating flow tends to be faster the nearer it is to the core, because of the conservation of angular momentum. Due to Coriolis effect from the Earth's self-rotation, typhoons circulate counterclockwise in the northern hemisphere and clockwise in the southern hemisphere.

The secondary circulation, illustrated in Fig. 3b, is the up-and-down overturning part of the typhoon's flow, providing the energy source to sustain its structure. A typhoon's primary energy comes from heat exchange between the evaporation of tropical ocean water and cooler outer space. The energetics of a typhoon system can be simplified as an ideal Carnot heat engine (Emanuel, 1986). When the near-surface wind reaches the typhoon eye's wall, it turns upward until it reaches the tropopause of the atmosphere. As a result, typhoon winds close to the eye wall have a noticeable upward vertical component. This has been observed and confirmed in several studies (Cao et al., 2009; Li et al., 2015).

Based on the typhoon structure, the authors examine the typhoon turbulence wind characteristics in the tangential and radial directions about the typhoon center, denoted as U and V , respectively, in Fig. 3a. The tangential component U presents primary horizontal rotation speeds, and the radial component V present the near ground airflow in radial direction.

5. Wind data characteristics

5.1. Mean wind speeds

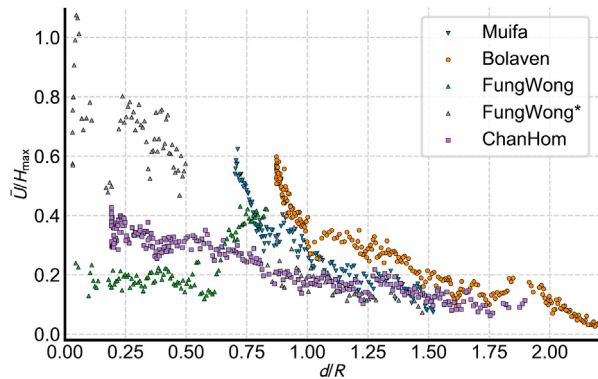
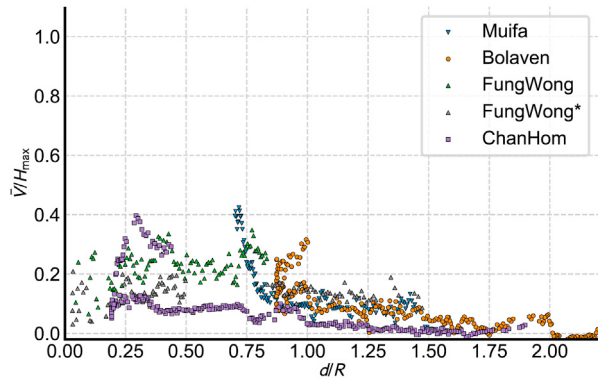
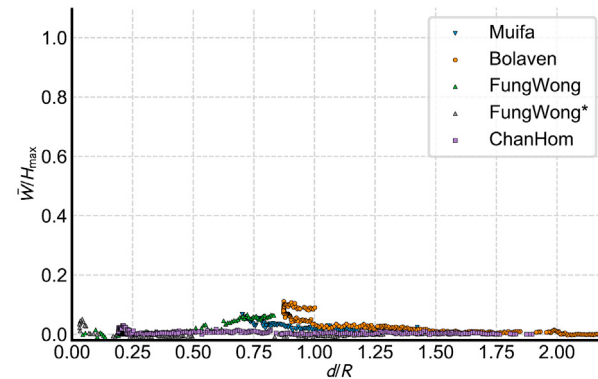
The original wind speeds from UAs are recorded in the north, east and vertical directions. First, wind speeds are divided into 10-min time intervals and then reprojected into the tangential U , radial V and vertical W direction according to the transient typhoon center at each time interval. Each typhoon center coordinates are extracted from IBTrACS. As the typhoon data in IBTrACS are normally recorded every 6 h, linear interpolation is used to determine the typhoon center for each 10-min interval.

The three wind components consist mean wind speeds \bar{U} , \bar{V} , \bar{W} parts and fluctuating parts u , v , w with zero-mean, shown in Eq. (1).

$$U = \bar{U} + u \quad (1a)$$

$$V = \bar{V} + v \quad (1b)$$

$$W = \bar{W} + w \quad (1c)$$

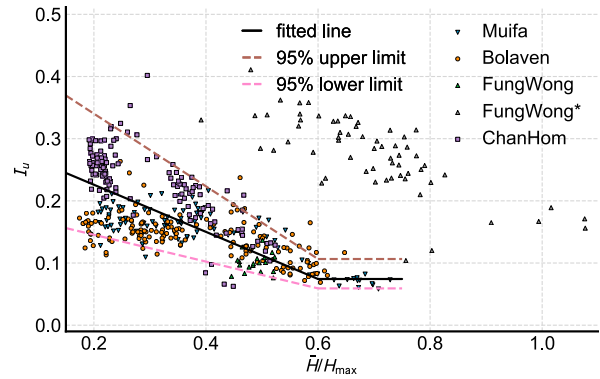
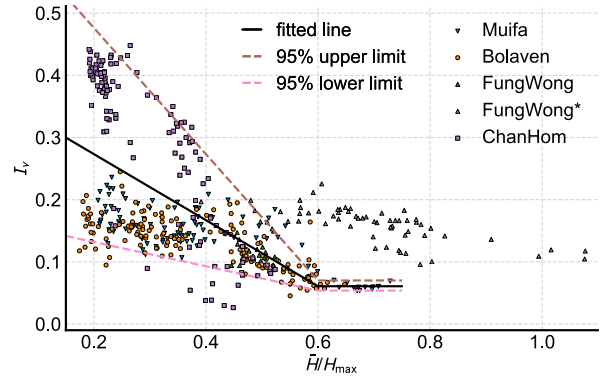
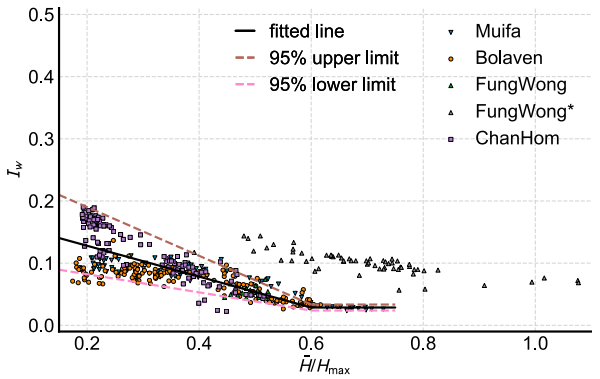
(a) Mean tangential wind speeds \bar{U} (b) Mean radial wind speeds \bar{V} (c) Mean vertical wind speeds \bar{W} **Fig. 7.** Relationship between mean wind speeds and typhoon internal structure.

where $\bar{[]}$ denotes the mean of wind speed components U, V, W during each 10-min interval.

Fig. 4 shows the variation of 10-min resultant mean wind speeds combining tangential, radial and vertical direction wind speeds components:

$$\bar{H} = \sqrt{\bar{U}^2 + \bar{V}^2 + \bar{W}^2} \quad (2)$$

in which $\bar{[]}^2$ is the square of corresponding mean components. Thus the corresponding zero-mean fluctuation parts are denoted as u, v, w and h . The start time of each typhoon data recording is 00:00 at September 6th' 2011 for typhoon Muifa, August 26th' 2012 for typhoon Bolaven, September 22nd' 2014 for typhoon Fung-Wong and July 10th' 2015 for

(a) Tangential direction: I_u (b) Radial direction: I_v (c) Vertical direction: I_w **Fig. 8.** Relationship between turbulence intensity and normalized mean wind speed.**Table 1**

Coefficients of double-line models for I_u, I_v, I_w .

a_j				b_j		
	\vee	\wedge	*	*	\vee	\wedge
u	-0.456	-0.792	-0.196	0.070	0.082	0.058
v	-0.391	-0.582	-0.144	0.058	0.069	0.054
w	-0.220	-0.331	-0.085	0.027	0.030	0.025

Notes (same as following tables).

*: Fitted values.

\vee : Values for 95% upper limit.

\wedge : Values for 95% lower limit.

typhoon Chan-Hom. The data labeled as invalid are removed from

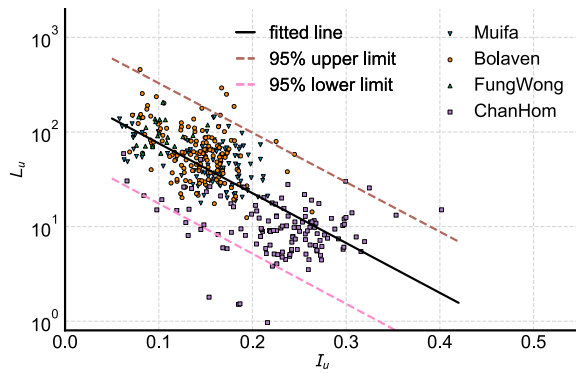
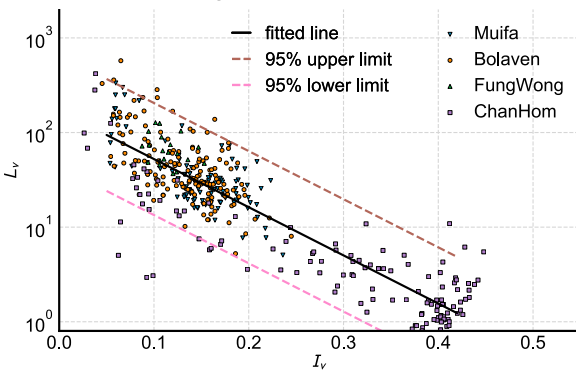
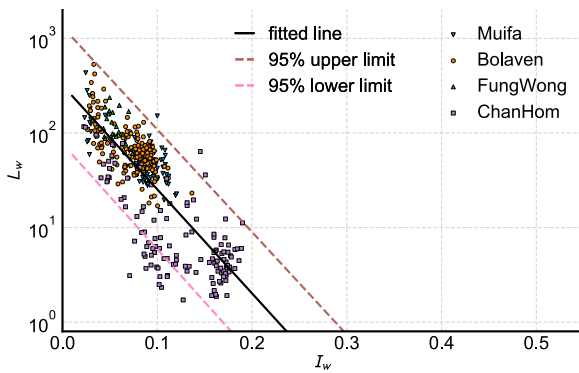
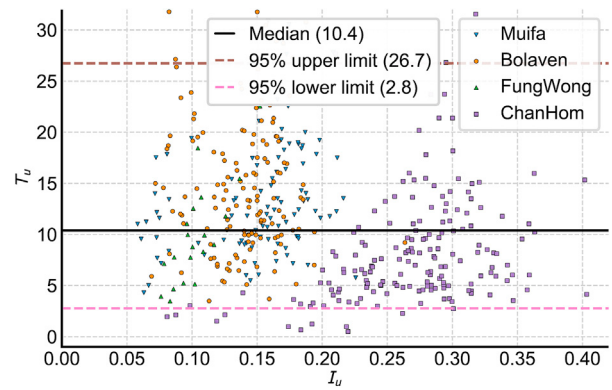
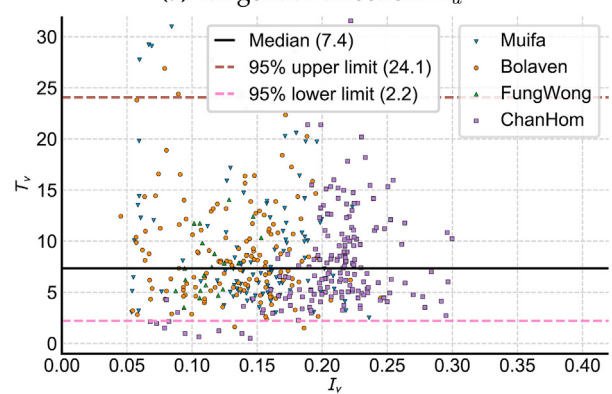
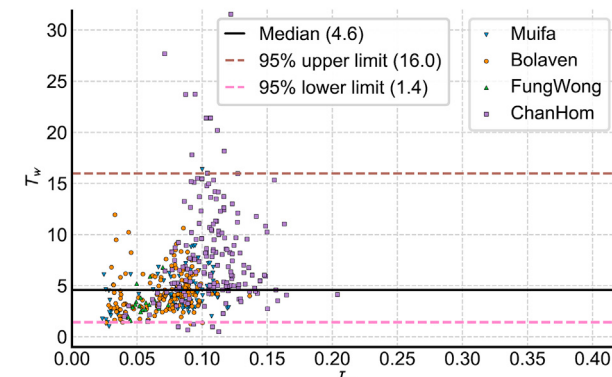
(a) Tangential direction: L_u (b) Radial direction: L_v (c) Vertical direction: L_w **Fig. 9.** Relationship between turbulence length scale and intensity.

Table 2
Coefficients of linear models for L_u , L_v , L_w .

	c_j		d_j			
	V	\wedge	*	V	\wedge	
u	-4.961	-4.947	-4.975	2.379	3.014	1.744
v	-6.986	-6.948	-7.024	2.450	3.306	1.864
w	-12.82	-12.45	-13.19	2.511	3.401	1.621

analysis in this study. Because typhoon Bolaven is one part of a twin typhoon system coupled with typhoon Tembin, only the first half data before it reached the closest location to Xihoumen Bridge are analyzed in this paper. Also, only the first half of the data of typhoon Chan-Hom are analyzed because it decayed very fast beyond 31°N, a little north of Xihoumen Bridge.

(a) Tangential direction: T_u (b) Radial direction: T_v (c) Vertical direction: T_w **Fig. 10.** Relationship between turbulence time scale and intensity.

The wind speeds and directios measured by UAs at three different locations for the four typhoon records are plotted in Figs. 4 and 5. For a certain duration, either northern anemometers (UA1, UA3 and UA5) or southern anemometers (UA2, UA4 and UA6) are used depending on the incoming wind flow direction. Fig. 4 shows that the wind speeds at three different locations match each other very well, and any one of them can present the wind speeds records at Xihoumen bridge. Because the main purpose of this study is examining the turbulence characteristics from typhoon winds at single location, and the correlation of turbulence at different locations is not analyzed in this paper. Also, for consistency in this study, the wind speeds from UA3 and UA4 at 1/2 span are employed since they locate at the middle span of Xihoumen bridge with the least interference effect from bridge cables and hangers.

Since the main objective of this study is the wind characteristics in the typhoon outer region, it is necessary to demonstrate the three-directional

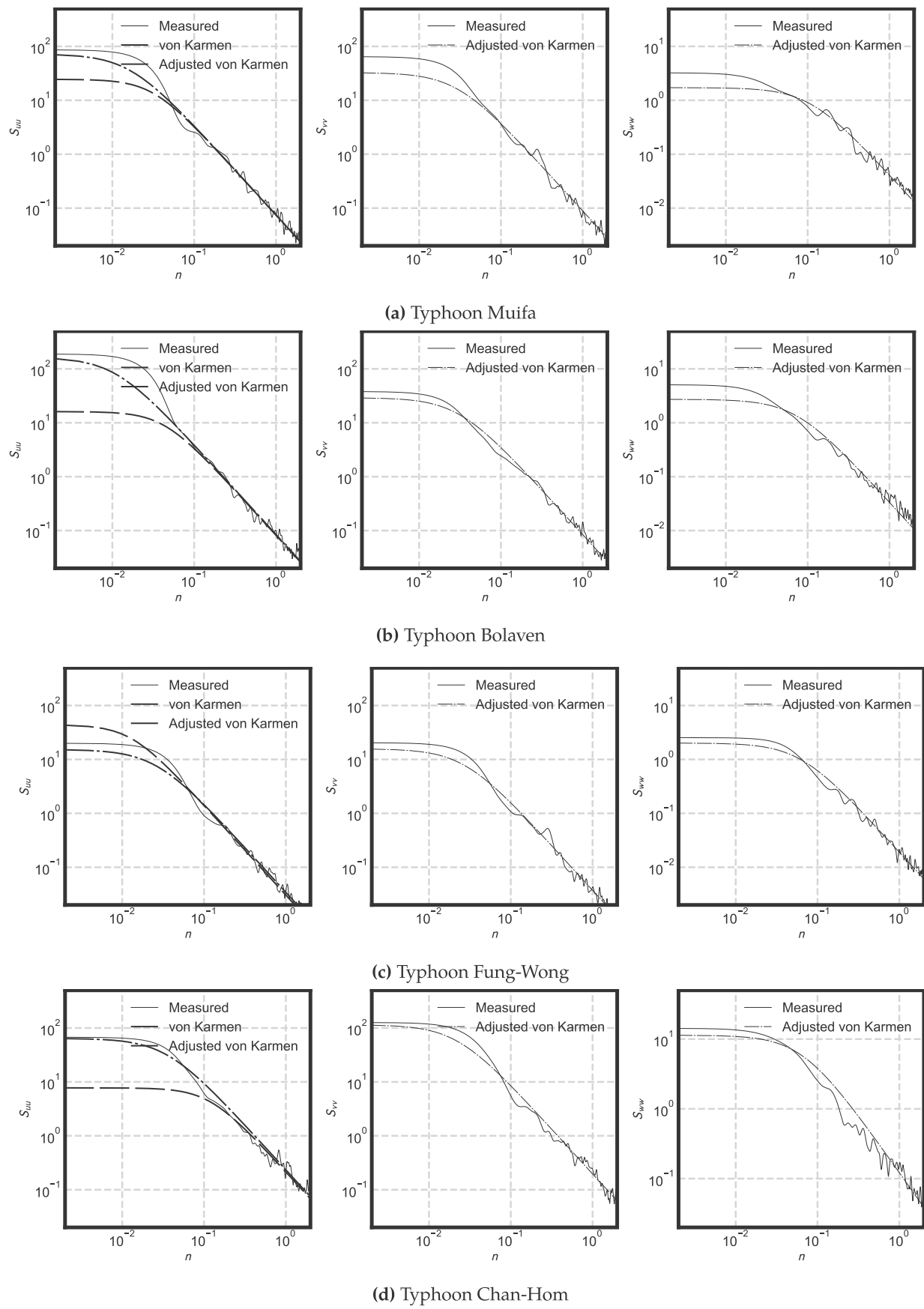
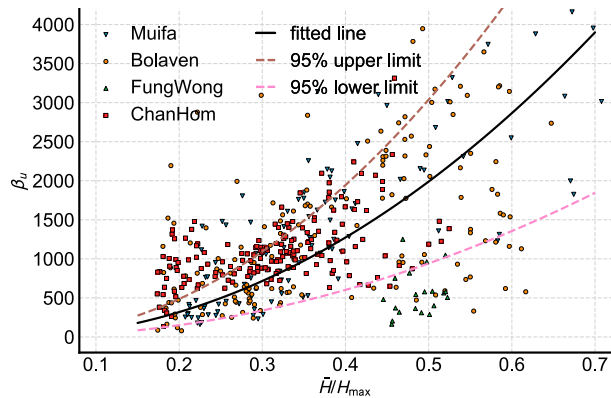
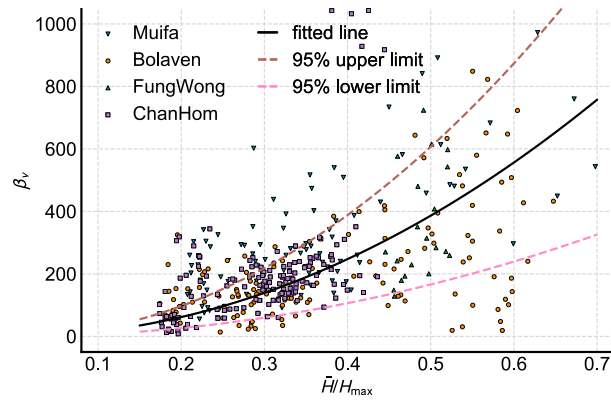
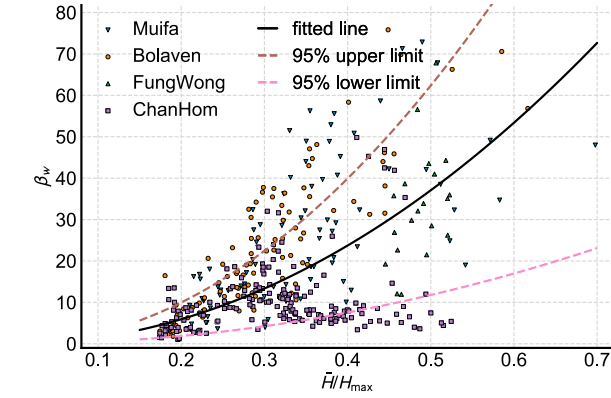


Fig. 11. Spectra of largest wind from four typhoon records.

(a) Tangential direction: β_u (b) Radial direction: β_v (c) Vertical direction: β_w **Fig. 12.** Variation of parameter β_j with normalized mean wind speeds \bar{H}/H_{\max} .

mean wind speeds at different locations inside the typhoon structure. In meteorology, the most common metrics used to quantify a typhoon's size is the radius of outermost closed isobar (ROCI). This is calculated from the average distances from the typhoon center to its outermost closed isobar in four quadrants, which are normally recorded in IBTrACS. Size plays an important role in modulating damage, but current research shows that a typhoon's size has little relation to its intensity (Chavas and Emanuel, 2010).

Like typhoon center coordinates, ROCI is also reported every 6 h, so ROCI for each 10-min interval is calculated by interpolation between the closest two recorded time steps in IBTrACS. Fig. 7 shows the mean wind speeds in three directions for four typhoon records. Because the different typhoon intensities and varying distances d from typhoons center to

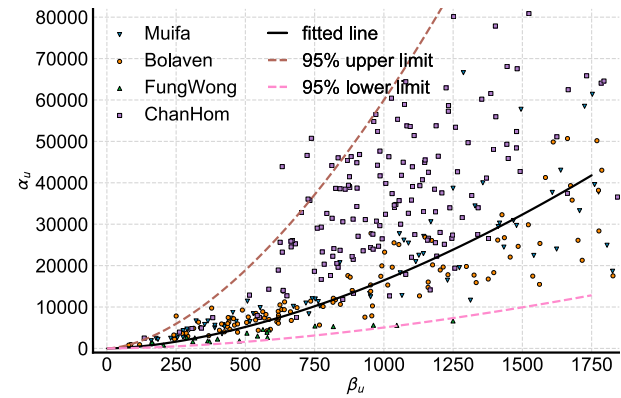
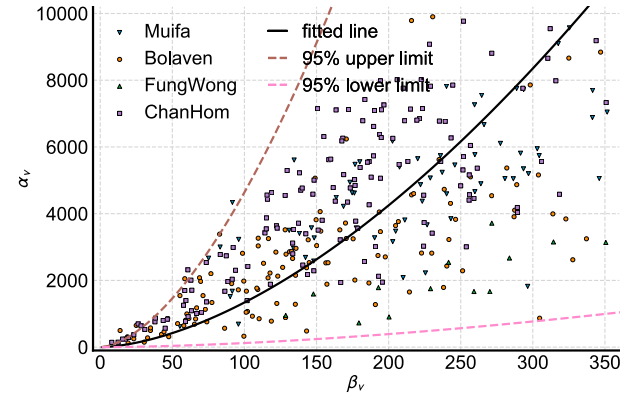
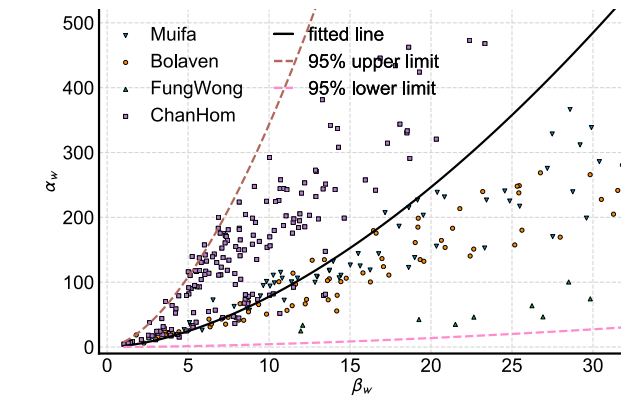
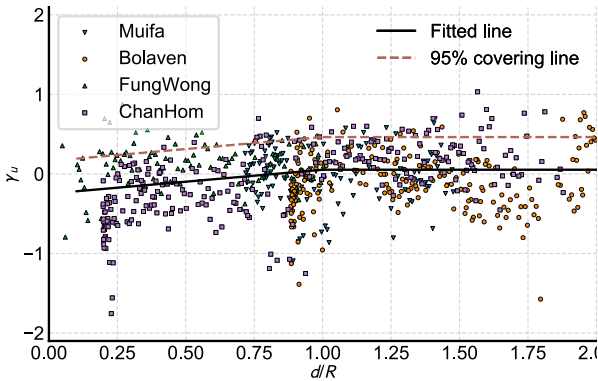
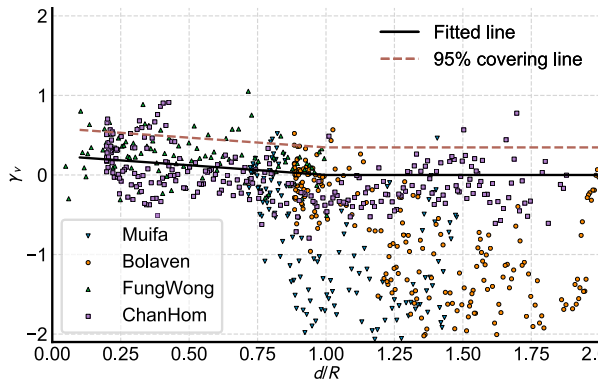
(a) Tangential direction: α_u (b) Radial direction: α_v (c) Vertical direction: α_w **Fig. 13.** Variation of parameter α_j with normalized mean wind speeds \bar{H}/H_{\max} .

Table 3
Coefficients of parabola models for β_u , β_v , β_w , α_u , α_v , α_w .

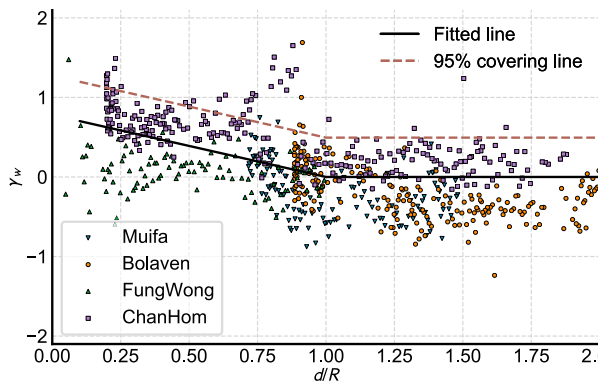
	e_j	f_j				
		V	A	*	V	A
u	0.339	0.736	0.167	7958	12152	3765
v	0.752	1.584	0.180	1546	2427	664.8
w	1.362	3.322	0.243	148.3	249.4	47.15



(a)



(b)



(c)

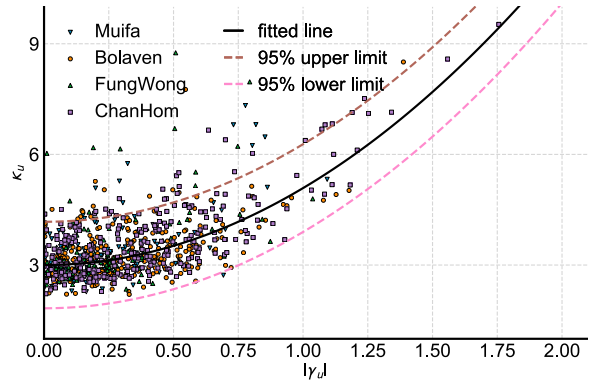
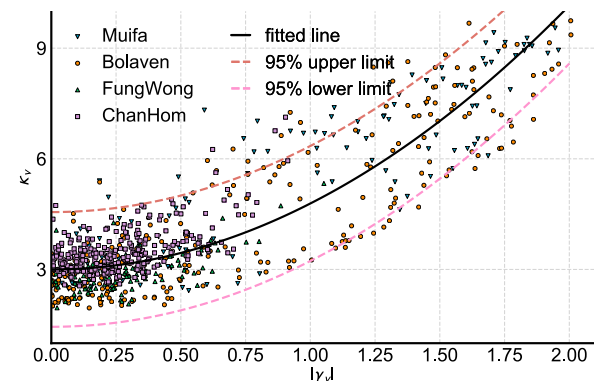
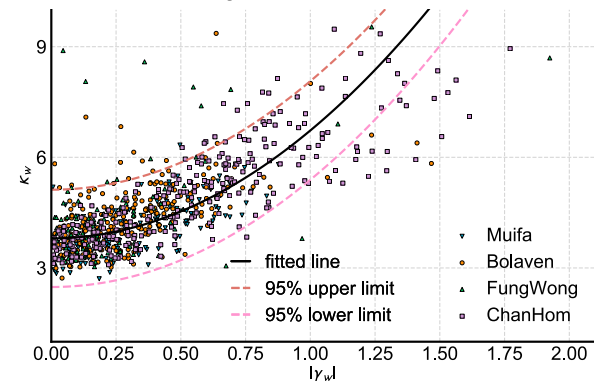
Fig. 14. Variation of turbulence skewness with relative distance to hurricane center.

Table 4

Coefficients of double-line models for turbulence skewness γ_u , γ_v and γ_w .

	g_j			h_j
		V	*	V
u	0.301	0.301	0.053	0.463
v	-0.245	-0.245	0	0.367
w	-0.781	-0.781	0.05	0.494

Xihoumen Bridge, d is normalized to typhoon size ROCI R and the 3 directional wind speeds are normalized to the typhoon maximum sustained wind speeds H_{\max} near typhoon center at corresponding time. H_{\max} is also reported in IBTrACS as the typhoon's intensity measure.

(a) Tangential direction: κ_u (b) Tangential direction: κ_v (c) Tangential direction: κ_w **Fig. 15.** Variation of turbulence kurtosis with absolute value of skewness.**Table 5**

Coefficients of parabola models for turbulence kurtosis κ_u , κ_v and κ_w .

	l_j			k_j		
		V	\wedge	*	V	\wedge
u	2.862	2.103	2.070	3.020	4.173	1.827
v	1.789	1.793	1.784	3.060	4.556	1.445
w	2.925	2.943	2.907	3.800	5.122	2.483

On average, the mean tangential wind speeds in Fig. 7a agree with the typhoon wind field model in Meng et al. (1995), derived from the conservation of angular momentum. \bar{U} drops very fast for $d < 0.5R$, but this decreasing trend of \bar{U} becomes small for larger d . Even for $d > R$, which is

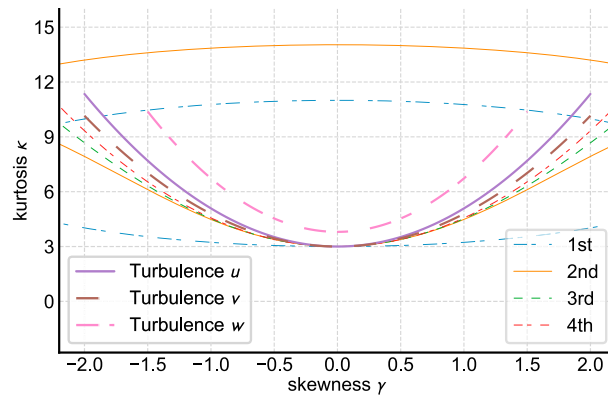


Fig. 16. Bounded skewness and kurtosis due to monotonic limits.

beyond typhoon dimension, there are still considerable tangential wind speeds around 20% of maximum typhoon speeds. For $d > 2R$, \bar{U} can be

considered as diminished. For time steps around typhoon Fong-Wong landed Xihoumen bridge site, the mean \bar{U} occasionally greater than reported maximum sustain wind speeds from typhoon database IBTrACS. During typhoon Fong-Wong landing, both maximum sustain wind speeds H_{\max} and recorded \bar{U} are relatively small. Therefore, \bar{U}/H_{\max} are sometime larger or close to 1 considering the unavoidable error in both typhoon database and UA recording.

The radial speeds \bar{V} in Fig. 7b are smaller than the tangential speeds, but \bar{V} remains roughly as constant around 15–20% of \bar{U} for $0 < d < R$. Beyond $d > R$, \bar{V} reduces rapidly to near 0.

The variation curves of \bar{U} and \bar{V} agree with the typhoon wind structure described in the previous section, and remain positive as predicted. Thus it is logical to decompose typhoon speeds into the tangential and radial directions about the typhoon centers.

Fig. 7c shows that vertical wind speeds are insignificant compared with \bar{U} and \bar{V} . Only typhoon Fung-Wong speeds have been recorded for the typhoon center, and its vertical wind speeds are around 5% of the maximum typhoon speeds. For most parts of its outer region, the vertical wind speeds are close to 0. The only exceptional part is at $0.7R < d < R$,

Table 6
Simulated typhoon turbulence characteristics.

	p (mbar)	d/R	H_{\max} (m/s)	\bar{U} (m/s)	\bar{V} (m/s)	I_v	L_v (m)	α_v	β_v	γ_v	κ_v
Case 1	920	0.2	63.0	34.4	6.88	0.075	84.1	22432	480.1	0.542	3.53
Case 2	920	0.3	63.0	22.7	4.53	0.152	24.6	21858	202.6	0.518	3.48
Case 3	950	0.2	50.09	33.5	6.70	0.059	101.0	43907	718.4	0.542	3.53
Case 4	950	0.3	50.09	22.6	4.52	0.116	43.64	46292	317.4	0.518	3.48
Case 5	980	0.2	34.84	26.0	5.20	0.059	110.0	63365	895.3	0.542	3.53
Case 6	980	0.3	34.84	16.0	3.19	0.114	44.97	47832	324.1	0.518	3.48

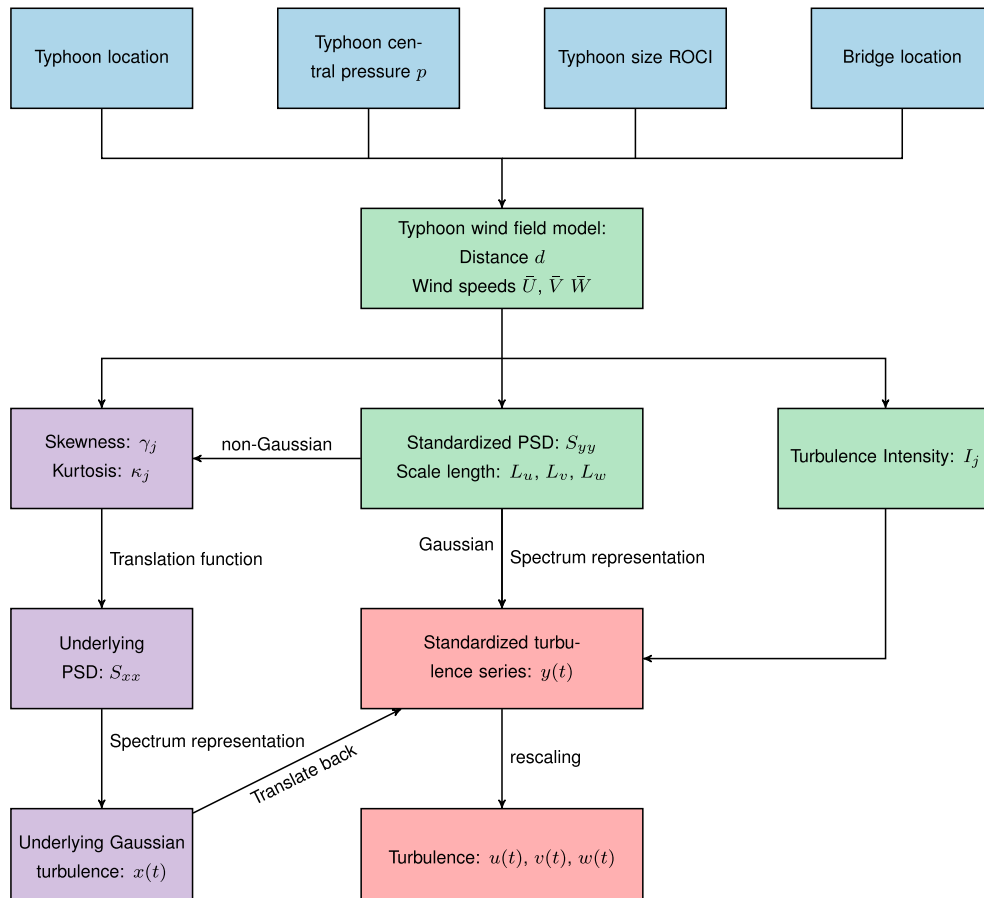


Fig. 17. Flow chart of typhoon wind turbulence simulation procedure.

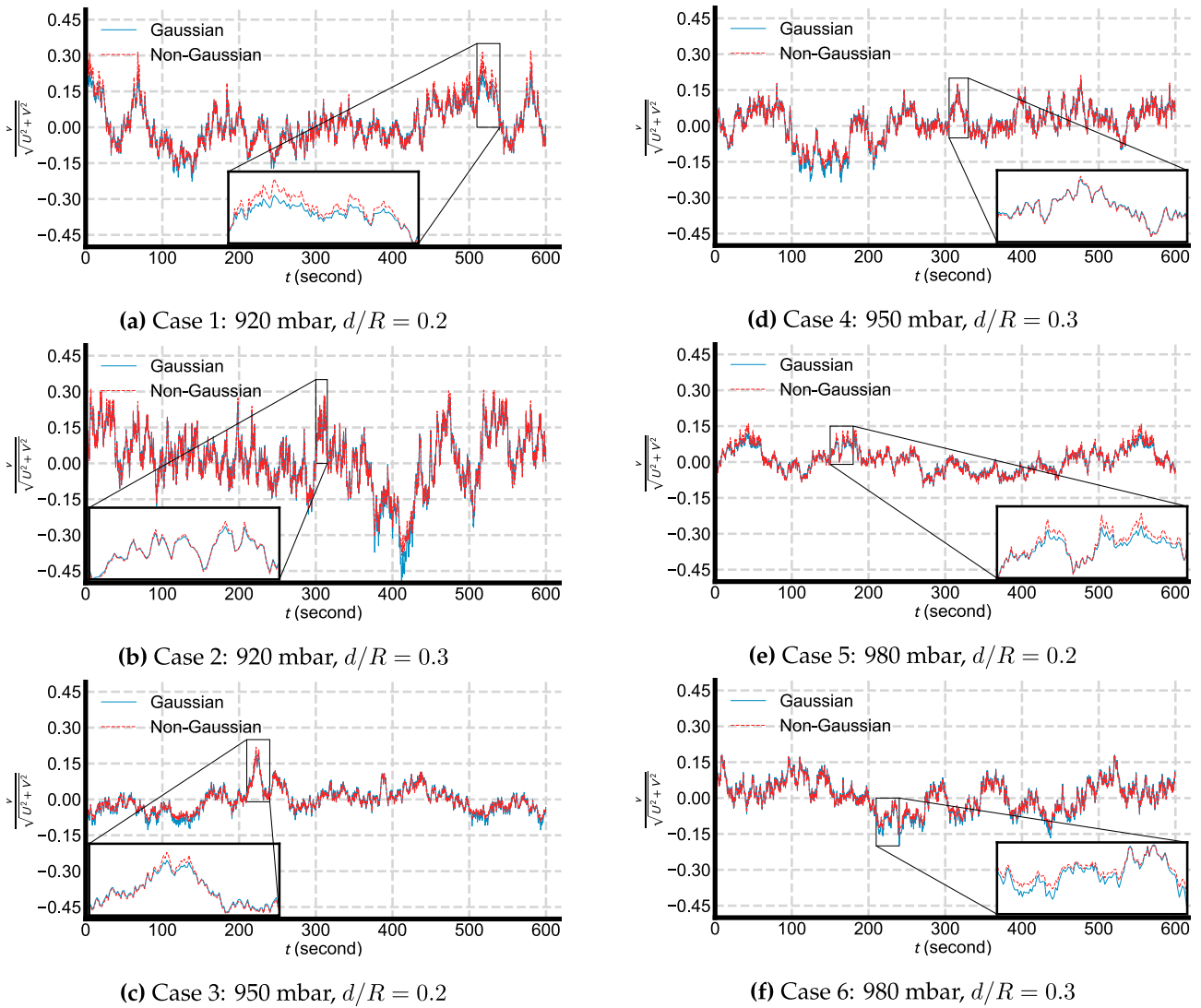


Fig. 18. Simulated Gaussian and non-Gaussian turbulences for 6 typhoon configurations.

where the vertical speeds indicate that noticeable convection exists at the some locations ($d/R < 1$) within the typhoon structure. This phenomena was decried in Frank (1977) as the vertical air convection is confined primary at the spiral bands. However, these observations need further investigation of typhoon structure at outer parts, and vertical wind speeds are insignificant and can be treated as 0 for engineering application, except in the eye wall region.

5.2. Turbulence intensity

Turbulence intensity for three wind speed components is defined as:

$$I_u = \frac{\sigma_u}{\bar{H}} \quad (3a)$$

$$I_v = \frac{\sigma_v}{\bar{H}} \quad (3b)$$

$$I_w = \frac{\sigma_w}{\bar{H}} \quad (3c)$$

where $\sigma_j = \sqrt{j^2}$ is the root mean square of turbulence, and j stands for u or v or w .

Fig. 8 shows the variations of tangential and radial turbulence

intensities I_u , I_v and I_w with resultant mean wind speed measured by UAs with 32 Hz sampling rate. In order to remove unavoidable noise, the original data are filtered by a low-pass filter with 5 Hz stop frequency.

Because the four typhoons had different intensities, the mean resultant wind speeds \bar{H} are normalized to maximum sustained wind speeds H_{max} near the typhoon center for the corresponding duration. To ensure turbulence data quality, the turbulence speeds with typhoon central pressures larger than 1000 mbar and $\bar{H} < 8$ m/s are removed from the following turbulence study in this section.

Of the 3 velocities I_u , I_v and I_w , I_u is the largest and its variance is also the greatest. Like the findings in Cao et al. (2009) and Li et al. (2015), the turbulence intensity has negative correlation with small mean wind speeds, and for larger mean wind speeds the turbulence tends to be constant. Identical correlation between I_u in Fig. 8a, I_v in Fig. 8b, I_w in Fig. 8c and the normalized wind speeds \bar{H}/H_{max} all confirm this. For $\bar{H}/H_{max} < 0.6$, all I_u , I_v and I_w decrease approximatively linearly with increasing wind speeds, while when $\bar{H}/H_{max} > 0.6$, all I_u , I_v and I_w remain at three different constant values. The abnormal cases all come from typhoon Fung-Wong before its landing, as indicated by gray triangles in Fig. 6 and labeled "Fung-Wong**". The moving path of typhoon Fung-Wong reveals that, before its landing, the wind blew from the southwest toward Xihoumen bridge and passed over rough land, which made the wind significantly more turbulent. All other typhoon wind blew

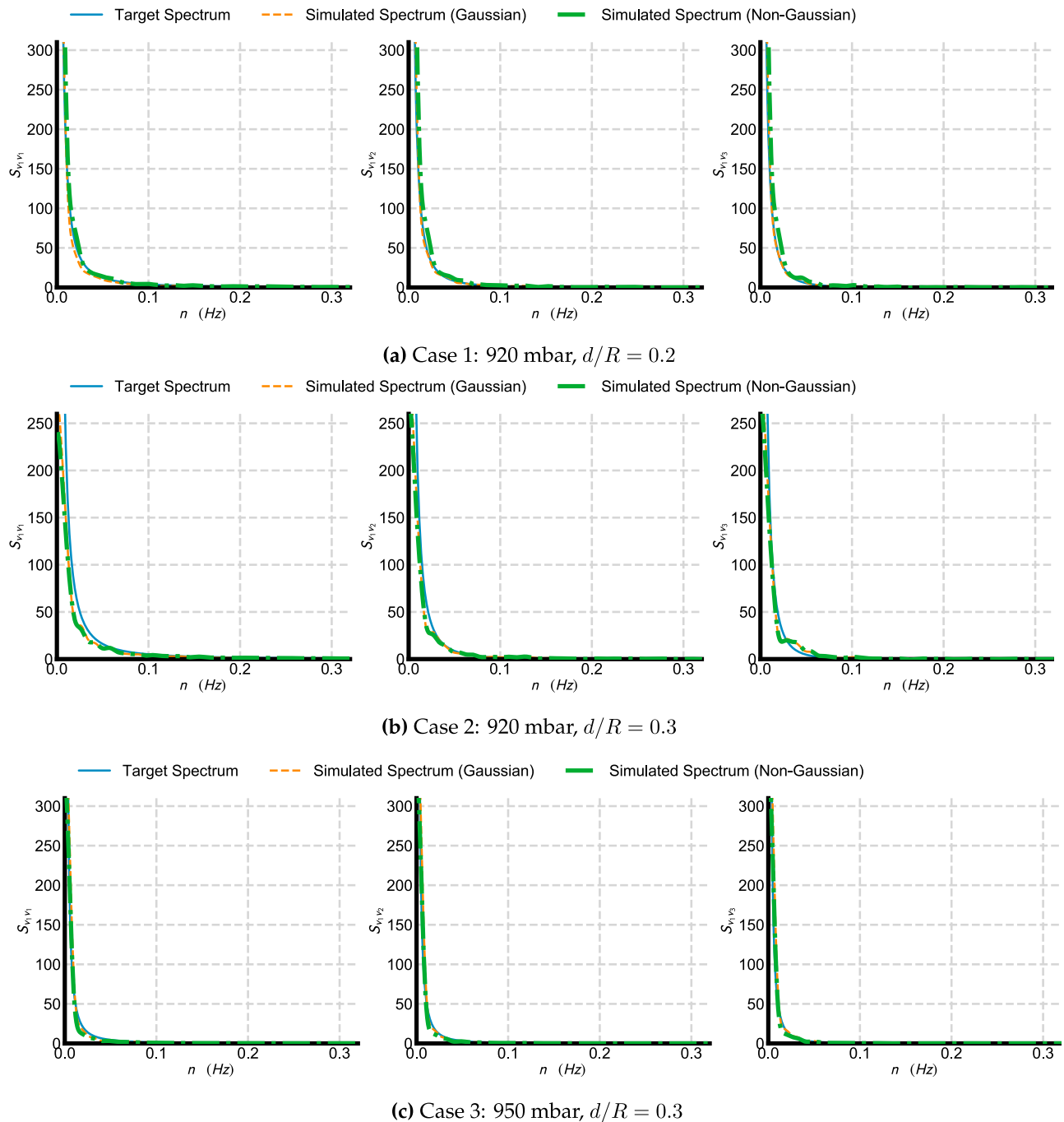


Fig. 19. Cross spectrum of Simulated Gaussian and non-Gaussian turbulences for 6 typhoon configurations.

from the northeast or southeast over smooth ocean.

Based on the above findings, a double-line model expressed by Eq. (4) is proposed to fit the relationship between three-directional turbulence intensity and normalized wind speeds.

$$I_j = \begin{cases} a_j \left(\frac{\bar{H}}{H_{\max}} - 0.6 \right) + b_j, & \frac{\bar{H}}{H_{\max}} < 0.6 \\ b_j, & \frac{\bar{H}}{H_{\max}} > 0.6 \end{cases} \quad (4)$$

where a_j, b_j are the coefficients to be determined, and $j = u, v, w$. Because of the higher turbulence of typhoon Fung-Wong, those data are not included in the linear fitting of Eq. (4). Table 1 shows the fitted double-

line model coefficients for I_u, I_v and I_w , and fitted lines are also shown in Fig. 8.

5.3. Turbulence length scale

Fig. 9 shows the variations of turbulence length scale with turbulence intensity in the corresponding direction. Different methods of calculating it also give significantly different results. Theoretically, the turbulence scale is defined as:

$$L_j = \frac{\bar{H}}{\sigma_j^2} \int_0^\infty R_j(\tau) d\tau \quad (5)$$

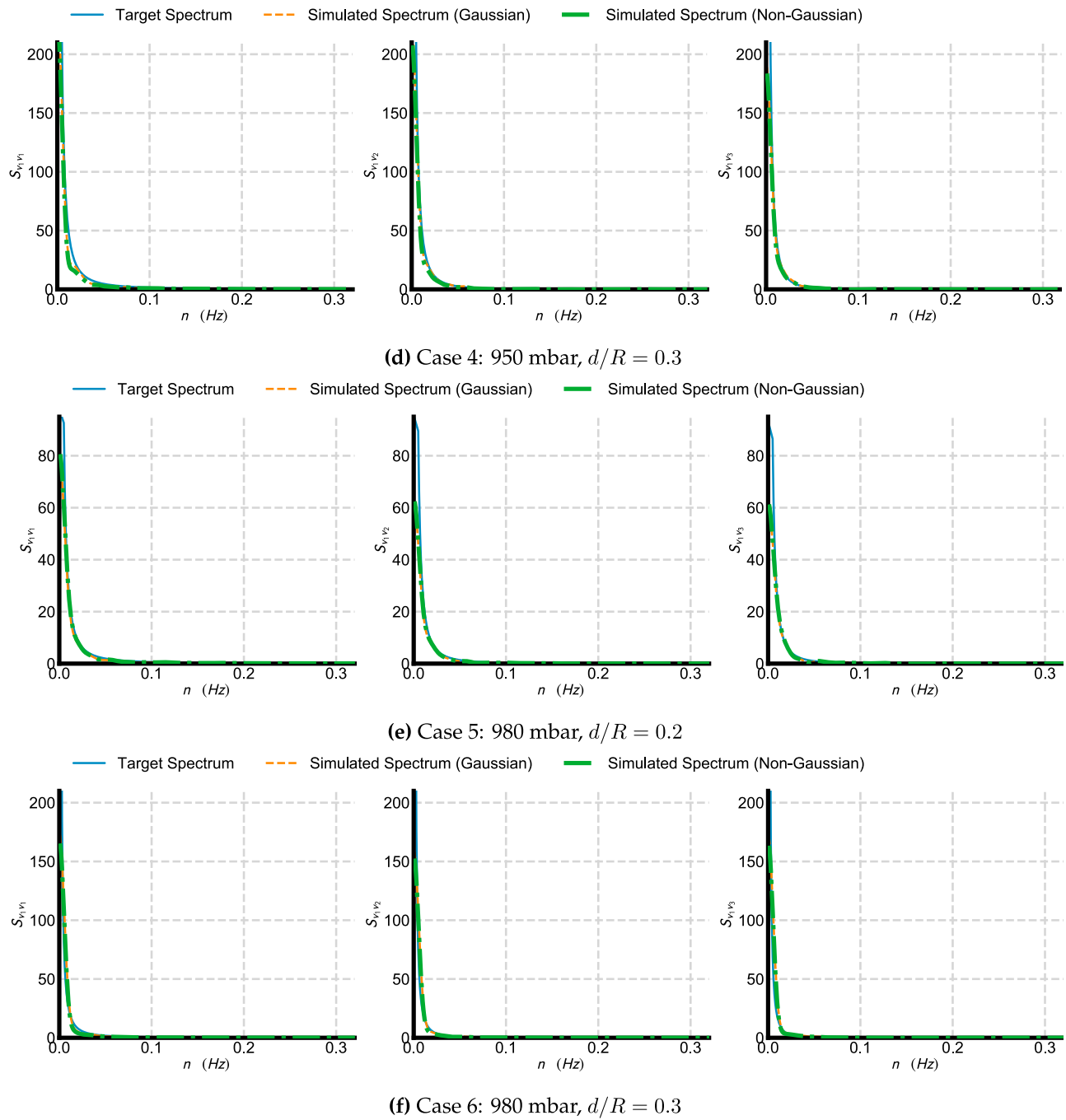


Fig. 19. (continued).

where \bar{H} is the resultant mean wind speed; $R_j(\tau)$ is the auto-covariance of each velocity component, u , v , w ; and σ_j^2 is the standard deviation of each fluctuating velocity component. In this study, in order to get a consistent estimation of the integral scale, the autocorrelation function $R_j(\tau)$ is integrated numerically from $\tau = 0$ to the first crossing of $R_j(\tau) = 0$.

It should be noted that some data points with very low integral length all come from Typhoon Chan-Hom records with very small wind speeds (8–10 m/s). Similar findings can be found in Cao et al. (2009).

Fig. 9 shows that turbulence scale varies greatly from several meters to hundreds meters, so L_u , L_v and L_w are plotted in logarithm scale. All three plots in Fig. 9 demonstrate that the logarithm of turbulence scale are roughly linearly correlated with turbulence intensity. The linear model expressed by Eq. (6), plotted as a black line in Fig. 9, and their

fitted coefficients are shown in Table 2.

$$\log_{10} L_j = c_j I_j + d_j \quad (6)$$

in where j stands for u or v or w .

The turbulence integral length scale calculated by Eq. (5) is transformed from integral time scale, defined as $T_j = \int_0^\infty R_j(\tau) d\tau$ based on Taylor's hypothesis of frozen wind flow (Simiu and Yeo, 2019). However, this hypothesis should be questioned for the low speed and high turbulence intensity scenarios, which are exactly the cases in typhoon wind environment. Thus, the integral time scale for three directional turbulence is plotted in Fig. 10. Unlike integral length scale L_j , T_j does not have clear relationship with turbulence intensity I_j . For tangential and radial direction, integral time scale T_u and T_v keeps around 10 s, and, for

vertical direction, integral time scale T_w is shorter around 5 s.

5.4. Turbulence spectrum

Although the power spectral density (PSD) is one of the key interesting points about typhoon wind turbulence, there is still no consensus on the general properties of different frequency bands. Cao et al. (2009) and Xu and Zhan (2001) showed that the power spectrums of typhoon winds generally follow a Kármán-type spectrum. On the other hand, added energies are noticed at low frequencies in several other studies, such as Yu et al. (2008) and Schroeder et al. (2009). At high frequencies, most research confirms that turbulence satisfies Kolmogorov's second hypothesis, in which the energy decreasing rate is $-5/3$.

Fig. 11 shows an example of a power spectrum of tangential u , radial v and vertical w velocity components of the strongest wind measured in each typhoon. The PSD is calculated by Welch's method (Welch, 1967) with 50% length overlapping and 6.25% length Hanning window function. The power spectrum of tangential turbulence u is compared with that given by the von Kármán spectrum model, as expressed by Eq. (7).

$$\frac{nS_{uu}}{\sigma_u^2} = \frac{4 \frac{nL_u}{H}}{\left[1 + 70.8 \left(\frac{nL_u}{H} \right)^2 \right]^{\frac{5}{6}}} \quad (7)$$

The comparison shows that the von Kármán spectrum cannot model the extra energy in the low frequency region, which again confirms the finding in Yu et al. (2008) and Schroeder et al. (2009). This additional energy at low frequency most likely come from the "storm" environment (Schroeder and Smith, 2003). This paper proposes an adjusted von Kármán type spectrum model, as expressed in Eq. (8).

$$\frac{nS_{jj}}{\sigma_j^2} = \frac{\beta_j \frac{nL_j}{H}}{1 + \alpha_j \left(\frac{nL_j}{H} \right)^{\frac{5}{3}}} \quad (8)$$

where j denotes either u , v or w ; β_j determines the PSD at 0 frequency and α_j controls the turning curves between stable energy at low frequency and decreasing energy at high frequency. The PSD curves obtained from the maximum wind speeds of the four typhoons in Fig. 11 show that Eq. (8) is flexible enough to fit PSD, including the extra energy at low frequency, for all three turbulence components S_{uu} , S_{vv} and S_{ww} .

Fig. 12 shows that β_j is correlated with normalized wind speeds \bar{H}/H_{\max} . The parabola model is expressed by Eq. (9)

$$\beta_j = e_j \left(\frac{\bar{H}}{H_{\max}} \right)^2 \quad (9)$$

which can approximately model the relationship between β_j and \bar{H}/H_{\max} , plotted as black line in Fig. 12. It is obvious that α_j is closely tied to β_j since in Eq. (8) in the high frequency range the ratio $\beta_j/\alpha_j^{5/3}$ determines the location of decreasing slope of the PSD curve. It is reasonable to assume that α_j is linearly correlated with $\beta_j^{5/3}$ as in Eq. (10). The fitted curves in Fig. 13 confirm this relationship.

$$\alpha_j = f_j \beta_j^{5/3} \quad (10)$$

The fitted coefficients in Figs. 12 and 13 are shown in Table 3.

5.5. Non-Gaussian features: skewness and kurtosis

The high-order properties of typhoon wind turbulence have not been the main concern of most previous studies. Cao et al. (2009) states that skewness and kurtosis are independent of wind speeds and are close to a standard Gaussian distribution. Li et al. (2015) showed that skewness and kurtosis have a weak correlation with turbulence intensity. In a

typhoon's structure, the tangential airflows are expedited as the wind flow spiral into the typhoon center because of the shorter radius. The radial airflows are accelerated by the nonuniform typhoon pressure field. Because of this, the turbulence is possibly correlated with the location of the typhoon structure.

The turbulence skewness and kurtosis is defines as:

$$\gamma_u = \frac{\overline{u^3}}{\sigma_u^3}, \kappa_u = \frac{\overline{u^4}}{\sigma_u^4} \quad (11a)$$

$$\gamma_v = \frac{\overline{v^3}}{\sigma_v^3}, \kappa_v = \frac{\overline{v^4}}{\sigma_v^4} \quad (11b)$$

$$\gamma_w = \frac{\overline{w^3}}{\sigma_w^3}, \kappa_w = \frac{\overline{w^4}}{\sigma_w^4} \quad (11c)$$

where $\overline{[\cdot]^3}$ and $\overline{[\cdot]^4}$ is turbulence third and fourth central moment.

Fig. 14 plots the variation of the skewness of three-directional turbulence with normalized distance d/R . Fig. 14a shows that tangential turbulence skewness γ_u increases when $d < R$, and then remains constant when $d > R$. Conversely, as shown in Fig. 14b, radial turbulence skewness γ_v decreases when $d < R$, and is unstable when $d > R$, and its variance is very large. Fig. 14c shows that vertical turbulence skewness γ_w has a much larger (sometimes over 1), positive skewness close to typhoon center. The averaging value decrease to 0 at $d = R$ then remain around 0 for $d > R$.

In order to model the variance of turbulence skewness, we propose to use a double-line model as expressed by Eq. (12) to quantify the relationship between turbulence skewness and normalized distance d/R , which are plotted as solid lines in Fig. 14. The skewness averages for tangential and vertical directional turbulences are close to 0. However, most negative skewness in the radial direction are associated with small mean radial wind speeds \bar{V} . Thus, it is conservative and practical to set h_j to 0 for $r \geq d$. The coefficients of the fitted double-line model are listed in Table 4.

Due to the large variances of turbulence skewness, it is not conservative to directly use the mean values from direct measurements results. This study suggests raising the double-line model in order to cover most possible cases, e.g. 95%. Thus one-side covering line for skewness is utilized rather than two-sides for other parameters. In other words, h_j should be increased to improve reliability against wind loadings. The raised h_j with 95% covering rate, represented as h'_j , are also listed in Table 4, and plotted as a dotted line in Fig. 14.

$$\gamma_j = \begin{cases} g_j \left(\frac{d}{R} - 1 \right) + h_j & r < d \\ h_j & r \geq d \end{cases} \quad (12)$$

When turbulence speeds distribution is either positively or negatively skewed from Gaussian distribution, its kurtosis is also affected since the skewed distribution includes more frequent extreme deviations. Thus, turbulence kurtosis and the absolute value of skewness are correlated as shown in Fig. 15. A parabola with initial kurtosis value k_j closely models the relationship between kurtosis κ_j and skewness γ_j , and the coefficients are shown in Table 5.

$$k_j = l_j |\gamma_j|^2 + k_j \quad (13)$$

The initial turbulence kurtosis k_u and k_v for the tangential and radial direction are very close to 3, which means turbulence without skewness can be assumed to follow a Gaussian distribution. However, the vertical turbulence initial kurtosis k_w is 3.80, and the probability distribution of vertical turbulence tends to be "narrower" than the Gaussian distribution.

It should be noted that, due to the unavoidable wind measuring errors, the above turbulence non-Gaussian features model involves large

uncertainty, which need further investigation. Nevertheless, the skewed turbulence records shown in Figs. 14 and 15 is unfavorable for structural wind-induced response, and it is worth more attentions for wind characteristics in typhoon climate.

6. Simulation of Non-Gaussian turbulence in typhoon wind field

The typhoon turbulence characteristics and correlation modeling among them were established in the previous section. It is shown in Section 5 that the non-Gaussian features of typhoon turbulence cannot be ignored, especially the radial and vertical directional ones. The process of simulating typhoon turbulence at multiple spatial points is presented in the second part of this paper. The simulation results of turbulence without Non-Gaussian characteristics will be also shown parallelly as a comparison reference.

6.1. Theoretical background

Cholesky's decomposition based spectral representation method is the cornerstone of multivariate Gaussian random process simulation methods, which were proposed by Shinozuka and Jan (1972) and Deodatis (1996). Later the fast Fourier transform (FFT) technique was introduced in Shinozuka (1974) to improve the computing efficiency. Nevertheless, Cholesky's decomposition is still normally the bottleneck of computation speed, and Cao et al. (2000) created a fast random process simulation method with explicit form for Cholesky's decomposition for multiple equally spaced spatial points. This method has been widely used for aerodynamic analysis of long-span bridges.

However, simulation of non-Gaussian processes is significantly more challenging. Grigoriu (1984) proposed a memoryless translation process theory, which is mathematical rigorousness and has broad engineering applicability. It utilizes a non-linear translation function to derive an underlying spectral density function with Gaussian distribution:

$$j(t) = g(x(t)) = F_j^{-1}(G_x(x(t))) \quad (14)$$

where $j(t)$ is a non-Gaussian random process, such as typhoon turbulence time series, $g(\cdot) = F_j^{-1}(G_x(\cdot))$ is the translation function and $x(t)$ is the translated Gaussian process. F_j and G_x are the cumulative density functions of $j(t)$ and $x(t)$ respectively. Normally, $j(x)$ is standardized as $y(t) = (j(t) - \bar{J})/\sigma_j$ in application, in which \bar{J} is the mean of process $j(t)$ and σ_j is the standard deviation.

The translation process method has been widely used to generate non-Gaussian processes. Recently, the digital-filter methods is employed to produce high fidelity turbulence for several simple cases in Bercin et al. (2018).

When the non-Gaussian CDF F_j is explicitly defined, $g(\cdot)$ is found by a numerical or analytical method. Besides, the Hermite polynomial is a suitable translation function (Yang and Gurley, 2015) when the high order moment statistics are predefined. For a softening process (with kurtosis larger than 3), the third-order Hermite function transformation is

$$y = g(x) = s[x + h_3(x^2 - 1) + h_4(x^3 - 3x)], s = \frac{1}{\sqrt{1 + 2h_3^2 + 6h_4^2}} \quad (15)$$

in which s is the scaling factor ensuring the unit standard deviation of y . The coefficients h_3 and h_4 can be found by different order Taylor expansion of the Hermite polynomial (Yang and Tian, 2015).

In order to determine a suitable Taylor expansion order, the relationship between typhoon turbulence skewness γ_j and kurtosis κ_j defined in Eq. (13) and Table 5 are plotted in Fig. 16 at a smaller scale.

It is clearly shown that all three modeled directional turbulence's γ_j and κ_j are all within the limit of the 4th order Taylor expansion, which is chosen to calculate c and d in this study.

The incompatibility problem between the non-Gaussian autocorrelation function and the power spectral density function is the main concern in the application of the translation process method. Before detailed discussion of this matter, it is necessary to revisit the Gaussian and non-Gaussian process simulation method.

According to Shinozuka and Jan (1972), the i -th correlated multivariate random Gaussian process $x_i(t)$ can be calculated by superposition of:

$$x_i(t) = \sqrt{4\pi\Delta n} \sum_{m=1}^i \sum_{l=1}^N |H_{im}(n_{ml})| \cos(2\pi n_{ml}t - \theta_{im}(n_{ml}) + \Phi_{ml}) \quad (16)$$

where N is the number of evaluated frequency points, which is should be sufficiently large. $\Delta n = n_{up}/N$ is the frequency increment, and n_{up} is the upper cutoff frequency. Φ_{ml} is the independent random phase angles. H_{im} is derived from Cholesky's decomposition of S_{xx} and θ_{im} is the complex angle of H_{im} .

For the non-Gaussian multiple points process $y_j(t)$, a bi-directional relationship between the non-Gaussian and underlying Gaussian processes can be established from the translation function (Yang and Gurley, 2015):

$$R_{y_j y_k}(\tau) = \int \int_{-\infty}^{\infty} \int_{-\infty}^{\infty} g_j(x_i) g_k(x_k) G(x_i, x_k; \rho_{x_i x_k}(\tau)) dx_i dx_k \quad (17)$$

$R_{y_j y_k}(\tau)$ is the cross auto-correlation function for the non-Gaussian processes $y_j(t)$ and $y_k(t + \tau)$, and can be determined by the Fourier transformation from the cross spectral density function $S_{y_j y_k}(n)$, and vice versa.

For application to bridge aerodynamics, Cao et al. (2000) points out that the turbulence evaluating points can be assumed to be equally spaced, and the turbulence field is uniform in the bridge longitudinal direction. As a result, the spectral density function of $S_{yy}(n)$ has same diagonal elements, and can be decomposed explicitly.

The autocorrelation function translation function in Eq. (17) is a single valued transformation, which maps each value of the Gaussian correlation $\rho_{x_i x_k}(\tau)$ defined over the interval [-1, 1] to a specific value of the non-Gaussian correlation $\rho_{y_j y_k}(\tau)$ in the interval $[\xi_{ik}^*, 1]$.

$$\xi_{ik}^* = s_i s_k (-1 + 2h_3 h_{3k} - 6h_4 h_{4k}) \quad (18)$$

If $\rho_{y_j y_k}(\tau) < \xi_{ik}^*$, no $\rho_{y_j y_k}(\tau)$ can be found through Eq. (17), which is the first incompatibility. From the cross spectral density function $S_{yy}(n)$, the auto-correlation function $\rho_{y_j y_k}(\tau) \geq 0$. Additionally, Yang and Gurley (2015) showed that for any combination of skewness and kurtosis, ξ_{ik}^* is always less than 0. As a result, $\rho_{y_j y_k}(\tau) \geq 0 \geq \xi_{ik}^*$. In other word, the first incompatibility doesn't exist for turbulence simulation on bridges.

The second incompatibility is that the underlying Gaussian process cross spectral density function $S_{xx}(n)$ is possibly non-positive definite. Therefore Cholesky's decomposition cannot be applied. In this case, an iterative approach in Shields et al. (2011) is used to obtain $S_{xx}(n)$.

6.2. Typhoon turbulence simulation examples

Xihoumen Bridge is also employed to illustrate typhoon turbulence simulation results. The important factors of the simulation are as follow:

- $L = 1650$ m
- Number of simulated points: $M = 50$
- Upper cut-off frequency: $n_{up} = 2$ Hz
- Number of simulated frequency points: $N = 1024$
- Time interval: $dt = 0.25$ s

A total 6 typhoon cases are assumed to be located due east (same latitude) of Xihoumen bridge with 3 different central pressure: 920, 950, 980 mbars and 2 different distances to the typhoon's center: 80, 120 km. The ROCI for all typhoons are assumed to be 400 km. For brevity, only

the radial direction turbulences are presented in this study. According to the turbulence characteristics measurements and modeling in Section 5, all necessary turbulence factors are listed in Table 6. The mean directional wind speeds on Xihoumen bridge and the maximum typhoon wind speeds are calculated by simplified hurricane wind field model in Vickery et al. (2000a), and the radial mean speeds \bar{V} are assumed to be 20% \bar{U} . It is should be noted that the wind field algorithm in Vickery et al. (2000a) may not be capable to accurate predict wind speeds for the northwestern Pacific typhoons, but this is not the main focus of this study. Any other alternative wind field model can be employed by the turbulence simulation procedure proposed in this study.

For comparison purpose, the Gaussian turbulence simulation results neglecting skewness and kurtosis are also presented parallelly. Fig. 17 shows the flow chart to calculate the Gaussian and non-Gaussian turbulences. Fig. 18 illustrates the time series for 6 different typhoon configurations. For comparison purpose, the random phase angel Φ_{ml} is same for Gaussian and non-Gaussian turbulence. Each non-Gaussian turbulences illustration in Fig. 18 clearly demonstrates the positive skewed features according to Fig. 14b: positive turbulence tends to be greater and negative turbulence tends to be smaller. For typhoon with moderate intensity, the turbulence has lower magnitude. For same typhoon intensity, turbulence intensity is also slightly weaker, but this trend is insignificant.

Fig. 19 shows cross-PSD function of Gaussian and non-Gaussian turbulence comparing against to target PSD, which is derived by adjusted von Kármán spectrum in Eq. (8) and coherence decay function. The first column shows the PSD for the turbulence on point 1 $S_{v_1 v_1}$ for 6 different typhoon cases. The second and third columns show the cross PSD between turbulences on point 1 and turbulence on point 2 and point 3 respectively, denoted as $S_{v_1 v_2}$ and $S_{v_1 v_3}$. The comparison in Fig. 19 demonstrates that Cholesky's decomposition based method can well simulate the Gaussian turbulence property on frequency domain, and furthermore the translation process function based method can sustain the PSD property and exhibit the skewed typhoon turbulence features.

7. Conclusions

Wind turbulence characteristics from four typhoons are presented on the basis of 10-min wind speed samples. The wind turbulence speeds are decomposed into tangential, radial and vertical direction according to the typhoon geographical location regarding target site. Results are summarized as follows:

1. Mean wind speeds generally decrease as the distance getting further from typhoon center. On tangential direction, mean wind speeds extended into the outside of typhoon periphery; oppositely, mean wind speeds on radial direction become insignificant. The vertical mean wind speeds mostly keep around 0 excepts near typhoon center and periphery edge.
2. Turbulence intensity decreases with wind speed and remains constant for larger wind speeds. A double-line model is proposed to present this relationship. Turbulence length scale exponentially decreases with turbulence intensity for all three directional turbulence.
3. Extra energies are noticed at the low-frequency region on power spectral density of all three directional turbulence, and an adjusted von Kármán spectrum with two parameters is introduced. Parameter β is parabolically increasing respect to normalized wind speeds, while parameter α is linearly correlated with $\beta^{3/5}$.
4. The non-Gaussian feature of typhoon wind turbulence is examined. Within the typhoon periphery, skewness varies differently regarding the distance to typhoon center; outside of typhoon periphery, the skewness is negligible and turbulence is more Gaussian-like as synoptic winds. Kurtosis is directly determined by skewness, and a parabola model is introduced to model their correlation.

On the second part of this paper, the Hermite polynomial based

translation function is employed to simulate non-Gaussian turbulence for 6 typhoon with different configurations. This method can well replicate the non-Gaussian features identified from field measurement, as well as sustain the desired PSD and cross PSD function. The comparison between non-Gaussian and Gaussian turbulence simulation shows that positive skewed turbulence tends to have higher extreme gust speeds, which is unfavorable for structural dynamic response within short time interval.

Acknowledgments

The authors gratefully acknowledge the support of Shanghai Pujiang Program (No. 19PJ1409800), National Key research and Development Program of China (2018YFC0809600, 2018YFC0809604) and National Natural Science Foundation of China (51678451). Any opinions, findings and conclusions or recommendations are those of the authors and do not necessarily reflect the views of the above agencies.

References

- Bercin, K.M., Xie, Z.T., Turnock, S.R., 2018. Exploration of digital-filter and forward-stepwise synthetic turbulence generators and an improvement for their skewness-kurtosis. *Comput. Fluids* 172, 443–466.
- Cao, S., Tamura, Y., Kikuchi, N., Saito, M., Nakayama, I., Matsuzaki, Y., 2009. Wind characteristics of a strong typhoon. *J. Wind Eng. Ind. Aerodyn.* 97, 11–21.
- Cao, Y., Xiang, H., Zhou, Y., 2000. Simulation of stochastic wind velocity field on long-span bridges. *J. Eng. Mech.* 126, 1–6.
- Chavas, D.R., Emanuel, K.A., 2010. A QuikSCAT climatology of tropical cyclone size. *Geophys. Res. Lett.* 37.
- Cui, W., Caracoglia, L., 2016. Exploring hurricane wind speed along US Atlantic coast in warming climate and effects on predictions of structural damage and intervention costs. *Eng. Struct.* 122, 209–225.
- Davenport, A.G., 1961a. The spectrum of horizontal gustiness near the ground in high winds. *Q. J. R. Meteorol. Soc.* 87, 194–211.
- Davenport, A.G., 1961b. A Statistical Approach to the Treatment of Wind Loading on Tall Masts and Suspension Bridges. Ph.D. Dissertation. University of Bristol, United Kingdom.
- Deodatis, G., 1996. Simulation of ergodic multivariate stochastic processes. *J. Eng. Mech.* 122, 778–787.
- Emanuel, K.A., 1986. An air-sea interaction theory for tropical cyclones. part I: steady-state maintenance. *J. Atmos. Sci.* 43, 585–605.
- Fang, G., Zhao, L., Cao, S., Ge, Y., Pang, W., 2018. A novel analytical model for wind field simulation under typhoon boundary layer considering multi-field correlation and height-dependency. *J. Wind Eng. Ind. Aerodyn.* 175, 77–89.
- Frank, W.M., 1977. The structure and energetics of the tropical cyclone I. storm structure. *Mon. Weather Rev.* 105, 1119–1135.
- Georgiou, P.N., 1986. Design Wind Speeds in Tropical Cyclone-Prone Regions. Ph.D. Dissertation. University of Western Ontario, London, Ontario, Canada.
- Grigoriu, M., 1984. Crossings of non-Gaussian translation processes. *J. Eng. Mech.* 110, 610–620.
- Kaimal, J., Wyngaard, J., Izumi, Y., Coté, O., 1972. Spectral characteristics of surface-layer turbulence. *Q. J. R. Meteorol. Soc.* 98, 563–589.
- Li, L., Kareem, A., Xiao, Y., Song, L., Zhou, C., 2015. A comparative study of field measurements of the turbulence characteristics of typhoon and hurricane winds. *J. Wind Eng. Ind. Aerodyn.* 140, 49–66.
- Masters, F.J., Tieleman, H.W., Balderrama, J.A., 2010. Surface wind measurements in three gulf coast hurricanes of 2005. *J. Wind Eng. Ind. Aerodyn.* 98, 533–547.
- Meng, Y., Matsui, M., Hibi, K., 1995. An analytical model for simulation of the wind field in a typhoon boundary layer. *J. Wind Eng. Ind. Aerodyn.* 56, 291–310.
- Mudd, L., Wang, Y., Letchford, C., Rosowsky, D., 2014. Hurricane wind hazard assessment for a rapidly warming climate scenario. *J. Wind Eng. Ind. Aerodyn.* 133, 242–249.
- Schroeder, J.L., Edwards, B.P., Giannanco, I.M., 2009. Observed tropical cyclone wind flow characteristics. *Wind Struct.* 12, 349–381.
- Schroeder, J.L., Smith, D.A., 2003. Hurricane Bonnie wind flow characteristics as determined from wemite. *J. Wind Eng. Ind. Aerodyn.* 91, 767–789.
- Sharma, R., Richards, P., 1999. A re-examination of the characteristics of tropical cyclone winds. *J. Wind Eng. Ind. Aerodyn.* 83, 21–33.
- Shields, M., Deodatis, G., Bocchini, P., 2011. A simple and efficient methodology to approximate a general non-Gaussian stationary stochastic process by a translation process. *Probabilistic Eng. Mech.* 26, 511–519.
- Shinozuka, M., 1974. Digital simulation of random processes in engineering mechanics with the aid of FFT technique(Fast Fourier Transformation). In: Stochastic Problems In Mechanics, pp. 277–286.
- Shinozuka, M., Jan, C.M., 1972. Digital simulation of random processes and its applications. *J. Sound Vib.* 25, 111–128.
- Simiu, E., Scanlan, R.H., 1986. Wind Effects on Structures: Fundamentals and Applications to Design, 2 ed. John Wiley & Sons, New Jersey, USA.
- Simiu, E., Yeo, D., 2019. Wind Effects on Structures: Modern Structural Design for Wind, 4 ed. Wiley–Blackwell, New Jersey, USA.
- Vickery, P., Skerlj, P., Twisdale, L., 2000a. Simulation of hurricane risk in the U.S. using empirical track model. *J. Struct. Eng.* 126, 1222–1237.

- Vickery, P.J., Skerlj, P., Steckley, A., Twisdale, L., 2000b. Hurricane wind field model for use in hurricane simulations. *J. Struct. Eng.* 126, 1203–1221.
- Von Karman, T., 1948. Progress in the statistical theory of turbulence. *Proc. Natl. Acad. Sci. U. S. A* 34, 530.
- Wang, X., Huang, C., Huang, P., Yu, X., 2017. Study on wind characteristics of a strong typhoon in near-ground boundary layer. *Struct. Des. Tall Special Build.* 26, e1338.
- Welch, P., 1967. The use of fast fourier transform for the estimation of power spectra: a method based on time averaging over short, modified periodograms. *IEEE Trans. Audio Electroacoust.* 15, 70–73.
- Xu, Y., Zhan, S., 2001. Field measurements of Gi Gang tower during typhoon york. *J. Wind Eng. Ind. Aerodyn.* 89, 73–93.
- Yang, L., Gurley, K.R., 2015. Efficient stationary multivariate non-Gaussian simulation based on a Hermite pdf model. *Probabilistic Eng. Mech.* 42, 31–41.
- Yang, Q., Tian, Y., 2015. A model of probability density function of non-Gaussian wind pressure with multiple samples. *J. Wind Eng. Ind. Aerodyn.* 140, 67–78.
- Yu, B., Chowdhury, A.G., Masters, F.J., 2008. Hurricane wind power spectra, cospectra, and integral length scales. *Boundary-Layer Meteorol.* 129, 411–430.
- Zhi, L., Li, Q., Wu, J., Li, Z., 2011. Field monitoring of wind effects on a super-tall building during typhoons. *Wind Struct.* 14, 253–283.